Six-Step Operation With Multistep Predictive Control Using the Trapezoidal Method for Traction PMSM Drives

Zhenyao Sun, *Student Member, IEEE*, Guanzhou Ren, Shuai Xu, *Member, IEEE*, Guangtong Ma, *Member, IEEE*, and Juri Jatskevich, *Fellow, IEEE*

***Abstract*—Model predictive control (MPC) has recently been considered for many permanent magnet synchronous motor (PMSM) drive applications. However, the conventional MPC presents insufficient overmodulation capability and, thus, cannot reach the six-step operation, which limits its application in the traction drive areas. This article proposes a novel MPC-based six-step operation scheme for the PMSM drive in traction applications. The prediction horizon is extended to the whole commutation period of the six-step operation, and a new average current-based objective function is introduced to determine the optimal commutation instants. To enhance the method's precision, a trapezoidal discretization method has been adopted in the long-horizon prediction. The effectiveness of the proposed method has been validated by detailed studies. The proposed method is demonstrated to have excellent current-tracking accuracy and fast dynamic response in the six-step operation, which is an advantage over the existing methods.**

***Index Terms*—Current prediction, model predictive control (MPC), permanent magnet synchronous machine, six-step, trapezoidal method.**

I. Introduction

PERMANENT magnet synchronous motors (PMSMs) have drawn increasing attention in railway traction applications, owing to their notable attributes of high efficiency and high power density [1], [2], [3]. As railway traction represents a prototypical medium-voltage, high-power drive application, the inverter switching frequency typically remains below 1 kHz. To further minimize the switching loss and enhance the dc-link voltage utilization, the high-speed region of railway traction PMSMs often necessitates the six-step operation [4], [5]. The six-step operation can maximize the utilization of the dc-link voltage by up to 10.27% compared with the linear modulation region, thereby extending the PMSMs highest speed ranges [6].

Field-oriented control (FOC), coupled with a variety of pulsewidth modulation methods, is widely employed for traction PMSMs. However, due to the voltage saturation, the current regulation ability of the conventional proportional–integral (PI) *dq* current controller with FOC will be degraded in the six-step operation. Extensive research has been conducted to address this issue, and a family of single-current controller methods has been proposed [7], [8], [9]. Nonetheless, these single-current methods often suffer from poor current dynamic performance and lose the tracking ability for the *q*-axis current. Some investigations have explored direct voltage angle control methods [10], [11], [12], [13]. In [12], the reference voltage angle is generated by a two-dimensional lookup table (2D-LUT) and is provided to generate the modulation voltage, but the current dynamics are not considered. In [13], the transient flux dynamics under the six-step operation are analyzed, and a time-optimal voltage vector transition method is proposed to eliminate the flux error.

Recently, model predictive control (MPC) has demonstrated remarkable potential in medium-voltage high-power drive applications, owing to its ability to handle multiobjective targets and exhibit fast dynamic performance [14], [15], [16]. The MPC can be categorized into two variants: the continuous control set MPC (CCS-MPC) and the finite control set MPC (FCS-MPC). The CCS-MPC adopts a quadratic program solver to handle the online constrained optimization problems and is coupled with a modulator to generate the gate signals, which can achieve the overmodulation by incorporating specific constraints in the optimization problem [17], [18], [19]. Nevertheless, the CCS-MPC algorithm is quite complicated, and the high computation expense also hinders its application. The FCS-MPC considers the nonlinear switching states of the inverter and can directly output the optimal voltage vector without the modulation stage, which presents superior dynamic performance than the CCS-MPC [20]. Due to its simple structure and intuitive design process, FCS-MPC has attracted more attention in PMSM

Manuscript received 27 July 2023; revised 13 October 2023; accepted 12 November 2023. Date of publication 20 November 2023; date of current version 26 January 2024. This work was supported in part by the National Natural Science Foundation of China under Grants U21A20168, 52107059, and 52277018, in part by the Natural Science Foundation of Sichuan Province under Grants 2023NSFSC1976, 2022NSFSC1898, and 2022NSFSC0447, in part by the Natural Science Foundation of Liaoning Province under Grant 2022-KF-24-01, and in part by the Fundamental Research Funds for the Central Universities under Grant 2682023CG009. *(Corresponding author: Guangtong Ma.)*

Zhenyao Sun, Guanzhou Ren, Shuai Xu, and Guangtong Ma are with the State Key Laboratory of Rail Transit Vehicle System, Southwest Jiaotong University, Chengdu 610031, China. (e-mail: sun_zy@my.swjtu.edu.cn; rgz@my.swjtu.edu.cn; sxu@swjtu.edu.cn; gtma@swjtu.edu.cn).

Juri Jatskevich is with the Department of Electrical and Computer Engineering, The University of British Columbia, Vancouver, BC V6T 1Z4, Canada. (e-mail: jurij@ece.ubc.ca).

Color versions of one or more figures in this article are available at https://doi.org/10.1109/TPEL.2023.3334207.

Digital Object Identifier 10.1109/TPEL.2023.3334207

drives. However, the conventional FCS-MPC exhibits minimal overmodulation capacity and thereby cannot maximize the dc-link voltage utilization, which potentially becomes a limiting factor in traction drives.

While some publications have investigated the extension of the speed range using the FCS-MPC [21], [22], [23], [24], few have addressed the six-step operation. An alternative way to achieve the six-step operation with the FCS-MPC is to add a heavy penalization on switching efforts [25], [26]. However, this will deteriorate the reference tracking performance, and the tuning process to find the optimal weighting factor can be time-consuming and costly. In [27], the FCS-MPC for railway application in the six-step operation was investigated, wherein a voltage vector clamping method was proposed to enhance the dc-link voltage utilization. However, clamping angle calculation necessitates the accurate conversion of the reference voltage based on the deadbeat manner, which heavily relies on the model accuracy regarding the parameter sensitivity and the noise component coupled in the current. Consequently, the current dynamic performance could be somewhat limited. In [28] and [29], the six-step operation using FCS-MPC with boundary is elaborated, where a rectangular current boundary is introduced to restrict the switching frequency within the overmodulation speed ranges. Nevertheless, determining the exact boundary value required to achieve fundamental switching frequency under the six-step operation could be exceedingly challenging in practical applications. In [30], a predictive torque control is proposed to accomplish the six-step operation, and a time counter is introduced to facilitate the switch transition at the appropriate turning angle.

Extending the prediction horizon length can significantly improve the control performance of FCS-MPC while exponentially increasing the computations in the optimization process [31], [32]. However, when the PMSM enters the six-step operation, the number of candidate voltage vectors is reduced to two, which provides the possibility to apply the multistep prediction and, thus, extends the FCS-MPC. A predictive current control scheme with a long prediction horizon for the six-step operation was first proposed in [33], wherein an objective function is formulated by using the average value of the predicted current. However, in this yearly work, the current-tracking performance has not been analyzed, and the validation is made by the simulation only.

In this article, a novel FCS-MPC scheme is proposed that extends to the six-step operation for traction PMSM drives, which is based on the method in [33]. This method effectively enhances the overmodulation capability of the conventional FCS-MPC, thereby increasing the dc-link voltage utilization and broadening the speed range of the PMSM drive. The experimental test results validate the effectiveness of the proposed method. The novelty and contribution of this article can be summarized as follows.

1) A new cost function based on the average value of current is derived to achieve the six-step operation with FCS-MPC. The multistep prediction is introduced to calculate the average value of current over a long commutation period.
2) To improve the prediction accuracy with a six-step operation, the trapezoidal discretization method is introduced. Although the trapezoidal method for the MPC in the linear speed range has been studied in the literature [34], its performance with MPC in the six-step operation has not been studied yet. A detailed analysis has been conducted to evaluate the advantages of the trapezoidal method over the forward Euler method.
3) The experimental results demonstrate the effectiveness of the proposed method and the ability to transition smoothly between the linear and the six-step modes, which may not be possible with conventional MPC methods.
4) The proposed control method overall may be very useful for traction drives, enabling increased voltage utilization in the high-speed region.

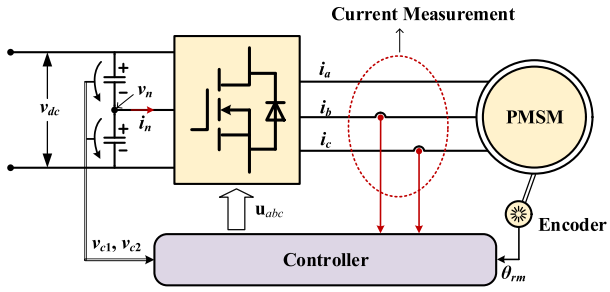

Fig. 1. Simplified circuit topology of a three-level inverter-fed PMSM drive.

II. System Modeling

A. Inverter and PMSM Model

Consider a simplified system circuit with a PMSM fed by a three-level inverter, such as the one depicted in Fig. 1. The switch position of the inverter can be defined as follows:

$$\mathbf{u_s} = [u_a \quad u_b \quad u_c]^T \tag{1}$$

where $\mathbf{u_s}$ represents the voltage vector in the stationary reference frame, and u_x $\{u_x \in (-1, 0, 1)\}$ denotes the normalized output voltage in phase x $\{x \in (a, b, c)\}$. Subsequently, there are 27 alternative voltage vectors for the three-level inverter. Then, the inverter output voltage in the rotating reference frame can be derived by

$$\mathbf{u_r} = \frac{1}{2} v_{\mathrm{dc}} \mathbf{K} \mathbf{u_s} \tag{2}$$

$$\mathbf{K} = \frac{2}{3} \begin{bmatrix} \cos\theta_r & \cos\left(\theta_r - \frac{2}{3}\pi\right) & \cos\left(\theta_r + \frac{2}{3}\pi\right) \\ -\sin\theta_r & -\sin\left(\theta_r - \frac{2}{3}\pi\right) & -\sin\left(\theta_r + \frac{2}{3}\pi\right) \end{bmatrix} \tag{3}$$

where $\mathbf{u_r} = [u_d \, u_q]^T$ represents the inverter output voltage in the rotating reference frame, and u_d and u_q are the corresponding dq-axis voltages. v_{dc} denotes the dc-link voltage. $\mathbf{K}$ is a matrix that transforms the variables in the abc-plane to the dq-plane based on the rotor electrical angle θ_r.

For the purpose of dc-link capacitor voltage balance, the neutral point potential should be maintained around 0, which is denoted by v_n and can be defined as

$$v_n = \frac{1}{2}(v_{c2} - v_{c1}) \tag{4}$$

where v_{c1} and v_{c2} are the measured voltages of the upper and lower capacitors of the dc side. The dynamics of the neutral point potential can be given as

$$\frac{dv_n}{dt} = -\frac{1}{2C_{\rm dc}} i_n \tag{5}$$

where $C_{\rm dc}$ represents the capacitance of dc bus; i_n denotes the neutral point current, which is determined by the phase current i_x $\{x\in(a, b, c)\}$; and the state of the switches captured by the normalized voltage state $u_x\in(-1, 0, 1)$. Based on the circuit in Fig. 1, i_n can be expressed as

$$i_n = \sum_{x\in(a,b,c)} (-i_x \,|u_x|). \tag{6}$$

The dynamic model of the PMSM based on the rotating dq reference frame can be described as

$$\begin{cases} u_d = R_s i_d + L_d \frac{di_d}{dt} - \omega_r L_q i_q \\ u_q = R_s i_q + L_q \frac{di_q}{dt} + \omega_r (L_d i_d + \psi_f) \end{cases} \tag{7}$$

where i_d and i_q are the stator currents; R_s is the stator winding resistance; L_d and L_q are the stator inductances; ψ_f is the flux linkage of the permanent magnets; and ω_r represents the rotor electrical angular speed. The electromagnetic torque T_e can be expressed as

$$T_e = 1.5 p i_q [(L_d - L_q) i_d + \psi_f] \tag{8}$$

where p represents the number of pole pairs in the PMSM.

B. FCS-MPC for Linear Speed Region

Based on the forward Euler method, (7) can be discretized and be expressed as state-space formulation, yielding

$$\mathbf{i_r}(k+1) = \mathbf{A}\mathbf{i_r}(k) + \mathbf{B}\mathbf{K}\mathbf{u_s}(k) + \mathbf{D} \tag{9}$$

where $\mathbf{i_r} = [i_d \; i_q]^T$ represents the stator current in the rotating reference frame; k is the time counter representing the sampling period. The matrices in (9) are given by

$$\mathbf{A} = \begin{bmatrix} 1 - \frac{R_s}{L_d} T_s & \frac{L_q \omega_r}{L_d} T_s \\ -\frac{L_d \omega_r}{L_q} T_s & 1 - \frac{R_s}{L_q} T_s \end{bmatrix}, \quad \mathbf{B} = \begin{bmatrix} \frac{T_s}{L_d} & 0 \\ 0 & \frac{T_s}{L_q} \end{bmatrix},$$
$$\mathbf{D} = \begin{bmatrix} 0 \\ -\frac{\psi_f \omega_r T_s}{L_q} \end{bmatrix} \tag{10}$$

where T_s denotes the sampling period.

According to (4)–(6), the neutral point potential can be predicted in the discrete formulation using the forward Euler method, yielding

$$v_n(k+1) = v_n(k) + \frac{T_s}{2C_{\rm dc}} [\mathbf{K}^{-1}\mathbf{i_r}(k)]^T \, |\mathbf{u_s}(k)| \tag{11}$$

where the notation for $|\mathbf{u_s}|$ is used to denote $[|u_a| \, |u_b| \, |u_c|]^T$ (which is not to be confused with the vector norm).

Next, the number of switch transitions should be established. For each lth vector candidate from the available set, the number of switching transitions of the inverter from its $(k-1)$th state to kth state is expressed as

$$\Delta\mathbf{u_s}(k) = \mathbf{u_s}(k) - \mathbf{u_s}(k-1) \tag{12}$$

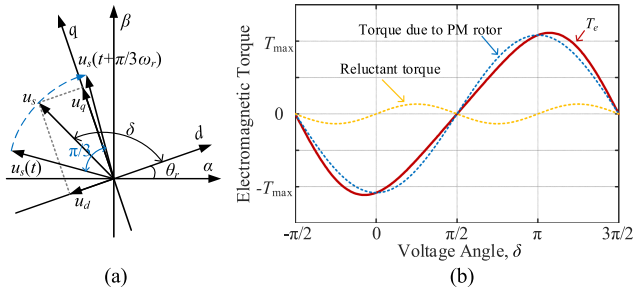

Fig. 2. (a) Definition of the voltage angle. (b) Electromagnetic torque curve versus voltage angle.

where $\Delta\mathbf{u_s}$ represents the change of voltage vector for each lth vector to be enumerated.

For the purpose of overall optimization, the system state at the $k+1$ instance is defined by

$$\mathbf{x}(k) = [\mathbf{i}_\mathbf{r}^T(k) \quad v_n(k) \quad \Delta\mathbf{u_s}(k)]^T. \tag{13}$$

The cost function of FCS-MPC is normally expressed by

$$J = (\mathbf{x}^*(k+1) - \mathbf{x}(k+1))^T \cdot \mathbf{w} \cdot (\mathbf{x}^*(k+1) - \mathbf{x}(k+1)) \tag{14}$$

where $\mathbf{w}$ represents a diagonal matrix consisting of weighting factors (WFs). Each variable in $\mathbf{w}$ represents a weight for the corresponding control target, which can adjust the priority of the control objectives. The superscript * denotes the variable with a reference value.

III. Analysis of Six-Step Operation

A. Voltage Angle

In the six-step operation, the amplitude of the fundamental component of the output stator voltage reaches its maximum value, which is

$$u_s = \frac{2}{\pi} v_{\rm dc} \tag{15}$$

where u_s is the output stator voltage. The definition of the voltage angle is presented in Fig. 2(a), where the voltage angle δ is defined as the angle (in radians) between u_s and the d-axis. The stator voltage in the dq frame can be given as

$$\begin{cases} u_d = u_s \cos\delta \\ u_q = u_s \sin\delta. \end{cases} \tag{16}$$

For the purpose of derivation, consider (7) in the steady state during the six-step operation. Then, by neglecting the resistive voltage drop, the steady-state stator current can be expressed as

$$\begin{cases} i_d = \frac{u_q}{L_d \omega_r} - \frac{\psi_f}{L_d} \\ i_q = -\frac{u_d}{L_q \omega_r} \end{cases} \tag{17}$$

Then, combining (8), (16) and (17), the electromagnetic torque can be derived as

$$T_e = -1.5p \left[\frac{\psi_f}{L_d \omega_r} u_s \cos\delta + \frac{L_d - L_q}{2 L_d L_q \omega_r^2} u_s^2 \sin 2\delta \right]. \tag{18}$$

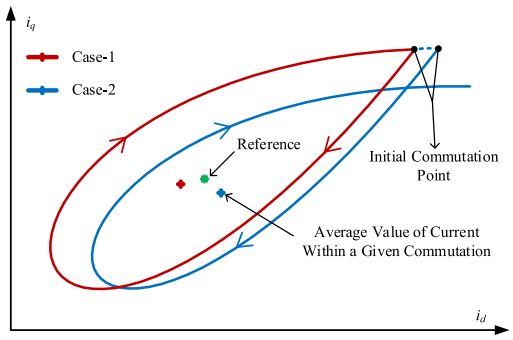

Fig. 3. Typical current trajectory in the *dq*-plane for a single commutation cycle with different commutation time instants: Case 1—applying new voltage vector immediately; and Case 2—applying the new voltage vector at the next sampling.

Since the amplitude of u_s is saturated under the six-step operation, the voltage angle becomes the only controllable variable to adjust the torque of the PMSM. The relationship between the electromagnetic torque and the voltage angle can be described by the curve, as shown in Fig. 2(b). Here, the dashed yellow line represents the reluctant torque, the blue dashed line represents the torque due to the PM rotor, and the red line represents the total resulting output electromagnetic torque T_e. As can be seen in Fig. 2(b), the voltage angle that corresponds to the minimum and maximum of the torque approximately equals 0 and π, respectively. Therefore, δ can be controlled in the approximate range of 0–π to adjust the electromagnetic torque monotonically. In the actual six-step operation, the voltage vector is applied for one-sixth of the fundamental period, and δ is the average value of the voltage angle. Hence, as the *dq* axes rotate, the actual voltage angle decreases from $\delta+\pi/6$ to $\delta-\pi/6$ over one commutation cycle, and then goes back to $\delta+\pi/6$ when the voltage is switched to the next voltage vector. The blue dashed line in Fig. 2(a) shows the movement of the voltage angle.

However, if one only adjusts the voltage angle in this simple step manner, the current dynamic response would be limited, and the current would have damped oscillations [5]. Alternatively, the dynamics of current should be considered to achieve a better performance under the six-step operation.

B. Current Trajectory

In the six-step operation, the current trajectory over any two adjacent commutation instants forms a waterdrop shape loop [4], as shown in Fig. 3. Depending on the rotor speed, the period for each commutation cycle may include a number of sampling intervals. Still, its general shape will be similar to the one depicted in Fig. 3. The red and blue lines show the current trajectories with different commutation points, where the commutation for the blue one is one sampling step later than the red one.

Since the voltage vectors are applied in sequence for the six-step operation, the new voltage vector to be applied depends on the present one. Thus, only two cases need to be considered in the objective function: Case-1 is to apply the new voltage vector immediately, while Case-2 is to apply the new voltage vector at the next sampling instant, as can be seen in Fig. 3.

Conventional MPC with one-step prediction will apply the voltage vector that achieves the closest distance of the predicted current at the next sampling instant and its reference value. However, the optimal voltage vector may not be correctly selected. Due to the voltage saturation, the *dq* current trajectory cannot be regulated directly to its reference. Instead, the optimal voltage regulates the *dq* current by the voltage angle, which will first decrease the *dq* current and then increase it, forming a waterdrop shape as the voltage angle changes. Assuming that the PMSM operates in a steady state, the current will trace the identical trajectory after each commutation instant. Hence, for each commutation cycle, the average value of the current should be equal to its reference (which is fixed in a steady state).

C. Control Problem Formulation

For the six-step operation, only the large voltage vectors are employed and are applied in sequence. Each vector lasts one-sixth of the period of the fundamental voltage. The voltage angle for the applied large vector decreases from $\delta^*+\pi/6$ to $\delta^*-\pi/6$ for ideal steady-state condition. However, the exact commutation instant will be determined by a current controller using the MPC to guarantee high dynamic current performance. When the actual voltage angle is close to $\delta^*-\pi/6$, the current controller will be activated to decide if the present voltage vector should be replaced with a new one or not.

In order to achieve precise and high dynamic current control for the six-step operation with the MPC scheme, the error between the average current over a commutation cycle and the reference current should be as low as possible, which yields the following objective function:

$$J = \frac{1}{T_p}\left\| \int_t^{t+T_p} \left[\mathbf{i}_\mathbf{r}^*(\tau) - \mathbf{i}_\mathbf{r}(\tau)\right] d\tau \right\|_2 \tag{19}$$

where t represents the initial time of the last commutation instant. We define the prediction horizon T_p, which represents the period of the commutation cycle under the six-step operation, given as

$$T_p = \frac{\pi}{3\omega_r}. \tag{20}$$

IV. Proposed Method

A. Objective Function

To determine the optimal commutation time instant, the average current for the entire current trajectory should be predicted, as given in (19). However, (19) should be discretized to be applied in the real-time microprocessor, which thereby requires multistep prediction. If the sampling time T_s is used as the time interval for each prediction step, the prediction steps would be extremely long, and thus, the computational cost may be too high to be implemented in the microprocessor. Hence, a limited number of steps should be employed to reduce the computational burden. Here, a subinterval for each prediction step denoted as

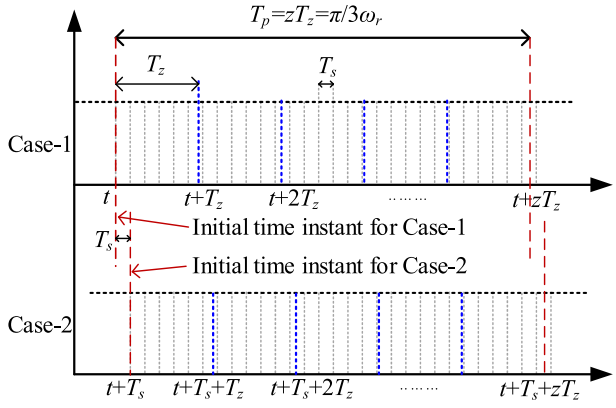

Fig. 4. Different subintervals inside the commutation cycle with period T_p.

T_z can be defined as

$$T_z = \frac{T_p}{z} \tag{21}$$

where z indicates the number of prediction steps (subintervals). The selection of z is presented in Section V-A, but it may be a reasonably small number of subintervals that still accurately reproduces the current trajectory in Fig. 3. Next, the original objective function described (19) can be discretized and expressed as

$$J = \left\| \mathbf{i}_\mathbf{r}^*(t) - \frac{1}{z}\sum_{i=1}^{z} \mathbf{i}_\mathbf{r}(t+iT_z) \right\|_2. \tag{22}$$

In (22), the reference current $\mathbf{i}_\mathbf{r}^*(t)$ is a constant within the prediction horizon. Meanwhile, it is noticed that the subinterval T_z is adopted for the average current calculation, which should be distinguished from the conventional MPC method.

The relationship between the sampling time and intervals (subintervals) is depicted in Fig. 4 for two cases. Case-1 corresponds to the commutation instants happening at time t, and in Case-2, the commutation occurs one sample interval later, at t+T_s. The real-time controller sets the sample interval T_s (length between two gray dashed lines), which is much shorter than T_z. The prediction horizon T_p (length between two red dashed lines, which also equals one commutation cycle) consists of z steps of the prediction subintervals T_z (distance between two blue dashed lines).

B. Current Prediction Using Trapezoidal Method

The current prediction for MPC is normally based on the forward Euler linearization method [20], which is given as

$$\mathbf{i}_\mathbf{r}(t+T_z) = \mathbf{i}_\mathbf{r}(t) + \frac{d\mathbf{i}_\mathbf{r}}{dt}(t)\cdot T_z. \tag{23}$$

Here, the current derivative is assumed to be constant during the time interval T_z. Based on (7), the current derivative can be calculated with the continuous state-space formulation as

$$\frac{d\mathbf{i}_\mathbf{r}}{dt}(t) = \mathbf{F}\mathbf{i}_\mathbf{r}(t) + \mathbf{G}\mathbf{u}_\mathbf{r}(t) + \mathbf{E} \tag{24}$$

where the state matrices are given as

$$\mathbf{F} = \begin{bmatrix} -\frac{R_s}{L_d} & \frac{\omega_r L_q}{L_d} \\ -\frac{\omega_r L_d}{L_q} & -\frac{R_s}{L_q} \end{bmatrix}, \quad \mathbf{G} = \begin{bmatrix} \frac{1}{L_d} & 0 \\ 0 & \frac{1}{L_q} \end{bmatrix},$$
$$\mathbf{E} = \begin{bmatrix} 0 \\ -\frac{\omega_r \psi_f}{L_q} \end{bmatrix}. \tag{25}$$

The forward Euler method can provide good calculation accuracy over a short-time interval. However, the time interval T_z could be prolonged if the number of prediction steps z is small. Therefore, a trapezoidal method is introduced to enhance the calculation accuracy for long-time intervals T_z. The trapezoidal method for current prediction is expressed as

$$\mathbf{i}_\mathbf{r}(t+T_z) = \mathbf{i}_\mathbf{r}(t) + \frac{1}{2}\left(\frac{d\mathbf{i}_\mathbf{r}}{dt}(t) + \frac{d\mathbf{i}_\mathbf{r}}{dt}(t+T_z)\right)T_z. \tag{26}$$

The dq current derivative for the (t+T_z) instant is unknown, which makes (26) an implicit equation that cannot be applied in the real-time calculation. The current derivative at the next time instant is given as

$$\frac{d\mathbf{i}_\mathbf{r}}{dt}(t+T_z) = \mathbf{F}\mathbf{i}_\mathbf{r}(t+T_z) + \mathbf{G}\mathbf{u}_\mathbf{r}(t+T_z) + \mathbf{E}. \tag{27}$$

For real-time calculations in a microcontroller, (27) should be expressed explicitly. The current state at (t+T_z) instant in (27) can be estimated using the forward Euler method given by (23). In this case, the output voltage at (t+T_z) instant should also be estimated iteratively with the time step T_z, as the voltage angle significantly changed within the long prediction horizon. Since $\mathbf{u_s}$ is fixed for the entire prediction horizon, the variation of $\mathbf{u_r}$ only depends on the voltage angle, which can be estimated as

$$\mathbf{u}_\mathbf{r}(t+T_z) = \frac{1}{2}v_{\mathrm{dc}}\mathbf{K}(t+T_z)\mathbf{u}_\mathbf{s}(t+T_z) \tag{28}$$

$$\mathbf{K}(t+T_z) = f(\theta_r(t+T_z)). \tag{29}$$

It is seen from (28) that the output voltage changes with the transformation matrix $\mathbf{K}$. The electrical angle θ_r(t+T_z) can also be calculated using the forward Euler method, yielding

$$\begin{aligned}\theta_r(t+T_z) &= \theta_r(t) + \dot{\theta}_r(t)T_z \\ &= \theta_r(t) + \omega_r T_z.\end{aligned} \tag{30}$$

Since the mechanical time constant is relatively larger than the electrical time constant, the rotor speed ω_r is seen as a constant in the whole prediction horizon.

The reference current for each subinterval can be derived by linear extrapolation, but some small reference oscillations might be amplified. In this study, the current reference is assumed to be the same as the initial value, which affects little to the current control accuracy.

As analyzed in Section III-C, only two cases need to be enumerated since the sequence of the voltage vectors has been determined for the six-step operation. Case-1 applies the new voltage vector immediately. Case-2 will keep the present voltage vector for one more sampling period T_s, and then apply the new voltage vector. The difference between the two conditions is the

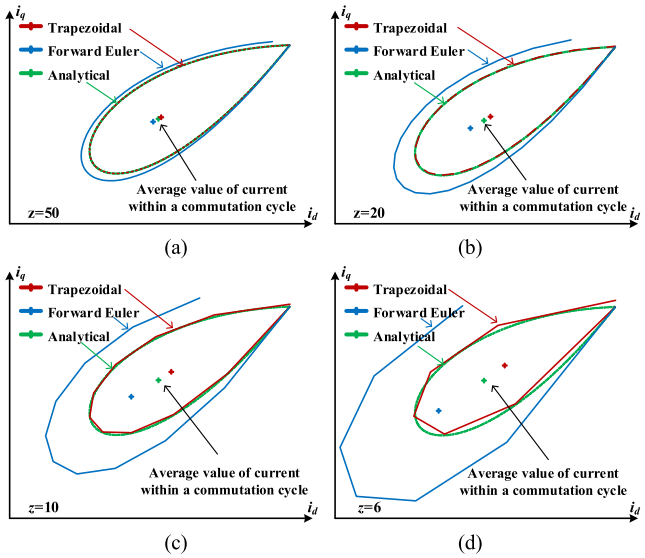

Fig. 5. Comparison of predicted current trajectory in the six-step operation using forward Euler and trapezoidal discretization methods for different numbers of prediction steps. (a) $z = 50$. (b) $z = 20$. (c) $z = 10$. (d) $z = 6$.

initial time. For Case-1, the initial time is t, and the initial current is the sampling current. For Case-2, the initial time is denoted by $t+T_s$, as seen in Fig. 5. Hence, the initial current for Case-2 can be given by

$$\mathbf{i_r}(t + T_s) = \mathbf{i_r}(t) + \frac{d\mathbf{i_r}}{dt}(t) \cdot T_s. \tag{31}$$

C. Voltage Angle Clamping

The voltage angle control enforces voltage angle clamping, which can hold the voltage vector unchanged until approaching the commutation instant. When the voltage angle is close to its reference, the MPC algorithm will be activated to decide the actual commutation instant. This mechanism can prevent the unexpected commutation, especially when the voltage angle is far from the exact reference commutation angle. The computation resources can also be released when the MPC is inactivated. It is noted that the voltage angle clamping does not decide the actual commutation instant. Thus, the optimal voltage vector can be expressed as

$$\mathbf{u}_{\text{opt}} = \begin{cases} \mathbf{u_s}(t), & \text{if } \delta^* - \delta < \frac{\pi}{6} + \varepsilon \\ \arg\min J, & \text{if } \delta^* - \delta \geq \frac{\pi}{6} + \varepsilon \end{cases} \tag{32}$$

where $\mathbf{u}_{\text{opt}}$ denotes the optimal voltage vector for the next control period, and ε is a defined value that affects the current-tracking dynamics.

The reference voltage angle δ^* can be calculated based on (18), but the calculation could be computationally expensive. The electromagnetic torque is related to the voltage angle and the electrical speed in the six-step operation, according to (18). Hence, a lookup table (LUT) method can be adopted to obtain the reference voltage angle [12]. Under a specific electrical speed, the torque can be adjusted monotonically by the voltage angle in a specific range. Since the outer speed loop feeds the reference stator current to the inner loop, the torque input of the LUT should be replaced by the current input, which can be estimated based on (8), assuming $i_d = 0$. Accordingly, a 2D-LUT block based on the electrical speed ω_r and the reference current i_s^* is introduced to obtain an approximate value of δ^*.

TABLE I
INITIAL VOLTAGE ANGLE FOR DIFFERENT VOLTAGE VECTORS

Voltage Vector	δ_{ini}
1, −1, −1	0
1, 1, −1	$\pi/3$
−1, 1, −1	$2\pi/3$
−1, 1, 1	π
−1, −1, 1	$4\pi/3$
1, −1, 1	$5\pi/3$

The present voltage angle δ can be derived according to the voltage vector. The six large voltage vectors correspond to the initial angles marked as δ_{ini}, as shown in Table I. The present voltage angle can be calculated as

$$\delta = \begin{cases} \delta_{\text{ini}} - \theta_r, & \text{if } \delta_{\text{ini}} \geq \theta_r \\ \delta_{\text{ini}} - \theta_r + 2\pi, & \text{if } \delta_{\text{ini}} < \theta_r. \end{cases} \tag{33}$$

D. Implementation of the Algorithm

The control algorithm of the proposed six-step MPC method consists of five steps, which are presented as follows.

Step 1: Check the rotor speed and determine the control mode of the MPC. Check the initial condition for six-step MPC. If the present voltage vector is not a large vector, calculate the optimal large vector with the linear MPC mode.

Step 2: Generate the reference voltage angle using 2D-LUT based on the rotor speed and reference torques. Calculate the voltage angle of the present voltage vector.

Step 3: Check if the present voltage angle is located in the clamping area. If yes, keep the same voltage vector output and skip to step 5. Else, go to step 4.

Step 4: Calculate the predicted current of two cases (see Fig. 3) within the prediction horizon T_p. Minimize the cost function and select the optimal voltage vector.

Step 5: Generate gate signals based on the optimal voltage vector and send them to the inverter.

V. PERFORMANCE ANALYSIS AND FULL-SPEED RANGE OPERATION

A. Current-Tracking Performance

To evaluate the prediction accuracy of the forward Euler and the trapezoidal methods, the predicted current trajectory with different numbers of prediction steps z (subintervals) is compared and presented in Fig. 5. When the number z decreases, the subinterval T_z becomes longer. Consequently, the prediction accuracy of the forward Euler method reduces significantly.

However, the current trajectory of the trapezoidal method nearly overlaps the analytical trajectory even for fairly large values of z. As a result, the prediction error of the average current

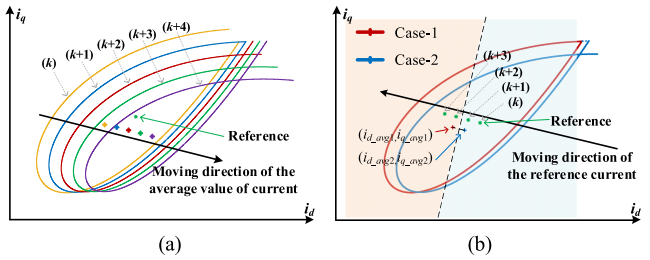

Fig. 6. Relationship between the average value of current and the current reference. (a) Current trajectories corresponding to delayed commutation instants while reference current is constant. (b) Moving reference current.

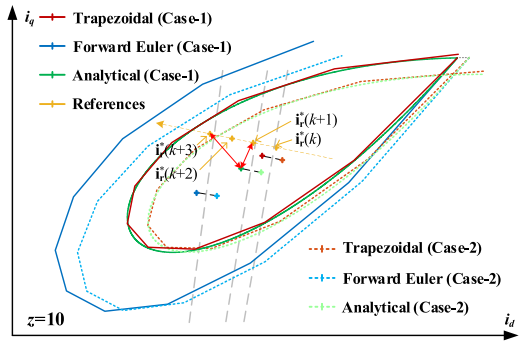

Fig. 7. Comparison of the commutation time instant of the forward Euler and trapezoidal methods.

with the trapezoidal method is significantly smaller than that for the forward Euler method.

To further analyze the current tracking in a practical application, the discrete nature of the MPC controller should be considered. Fig. 6(a) illustrates the moving direction of the average current as the commutation instant is delayed. As the commutation instant is incrementally delayed by sampling time T_s (from instant k to k+4), the current trajectory and its corresponding average value also change and shift to the right. In Fig. 6(a), the direction of the average current shift is indicated by the black arrow. In contrast, the reference current is assumed to stay constant for several sampling periods.

Another situation may be when the average current is assumed constant from one commutation cycle to the next, while the reference current may be stepping in some direction, as illustrated in Fig. 6(b). In this figure, the average current for Case-1 and Case-2 is assumed to be about the same for each sampling interval, and the reference current is moving along the direction indicated by the black arrow. Based on the average current values in Case-1 and Case-2, a midperpendicular of the two points can be plotted, which is shown in Fig. 6(b) with a dashed line. This line divides the plane into two parts, and it can be expressed as

$$\begin{aligned} y &= kx + b \\ k &= -\frac{i_{d\_\mathrm{avg1}} - i_{d\_\mathrm{avg2}}}{i_{q\_\mathrm{avg1}} - i_{q\_\mathrm{avg2}}} \\ b &= \frac{(i_{d\_\mathrm{avg1}} + i_{d\_\mathrm{avg2}})(i_{d\_\mathrm{avg1}} - i_{d\_\mathrm{avg2}})}{2(i_{q\_\mathrm{avg1}} - i_{q\_\mathrm{avg2}})} + \frac{i_{q\_\mathrm{avg1}} + i_{q\_\mathrm{avg2}}}{2} \end{aligned} \tag{34}$$

where i_{d_avg1} and i_{d_avg2} and i_{q_avg1} and i_{q_avg2} represent the average values of the d-axis current and q-axis current over a commutation interval, respectively. According to the objective function (11), the voltage vector switches only when the reference is geometrically closer to the average current value in Case-1. When the current reference moves to the left side of the midperpendicular, we have $i_q^* > ki_d^* + b$. Then, the voltage vector will be switched to the next one.

Based on Figs. 5 and 6, a typical current trajectory computed using different discretization methods is illustrated in Fig. 7, where the number of prediction steps z equals 10. In Fig. 7, the reference current point is assumed to step to the left along the yellow arrow. Here, the present-time instant is denoted by k. Based on this figure, it can be inferred that the commutation instant of the trapezoidal method will be (k+1), while for the forward Euler method, it will be (k+3) commutation instant.

According to Fig. 7, there will be a steady-state tracking error between the current reference and the predicted average current. These errors are marked with the red lines in Fig. 7. The distance between $\mathbf{i}_\mathbf{r}^*(k+1)$ and the analytical average current value of Case-1 (shown by the green point) indicates the actual tracking error. Likewise, the distance between $\mathbf{i}_\mathbf{r}^*(k+3)$ and the green point is the actual tracking error for the forward Euler method. Fig. 7 clearly illustrates that the tracking error for the trapezoidal method is primarily reduced (in both the d and q axes) compared with the forward Euler method.

The number of prediction steps z should be large to have a better control performance. However, considering the heavy computational burden on the real-time controller, the number z must be limited to several steps that can be completed within a single commutation instant. After investigation using simulations and experiments, it was determined that $z = 10$ (as in Fig. 7) gives good results for the considered experimental hardware.

B. Operation in the Full-Speed Range

The block diagram of the proposed MPC method is shown in Fig. 8, where the PI speed controller, the 2D-LUT, the reference calculation block, the dual-mode MPC, and the mode selection block are illustrated. The PI speed controller calculates the reference current i_s^* and provides it to the reference calculation block, which then assigns i_s^* to the dq frame and derives $\mathbf{i}_\mathbf{r}^*$. The 2D-LUT block feeds the reference voltage angle to the mode selection block, which decides the operation mode of the MPC controller. The MPC algorithm calculates the optimal voltage vector considering the selected operation mode and provides it to the inverter. In the mode selection block, a hysteresis controller based on the rotor speed and voltage angle is designed to guarantee a smooth transition between linear mode and six-step mode.

This article adopts the rotor speed and the reference voltage angle to determine the operating mode. Specifically, the rotor speed ω_{rm} is compared with a base speed ω_b, and the reference voltage angle δ^* is compared to 90°. To prevent frequent changes between the operating modes at the margin values, a small

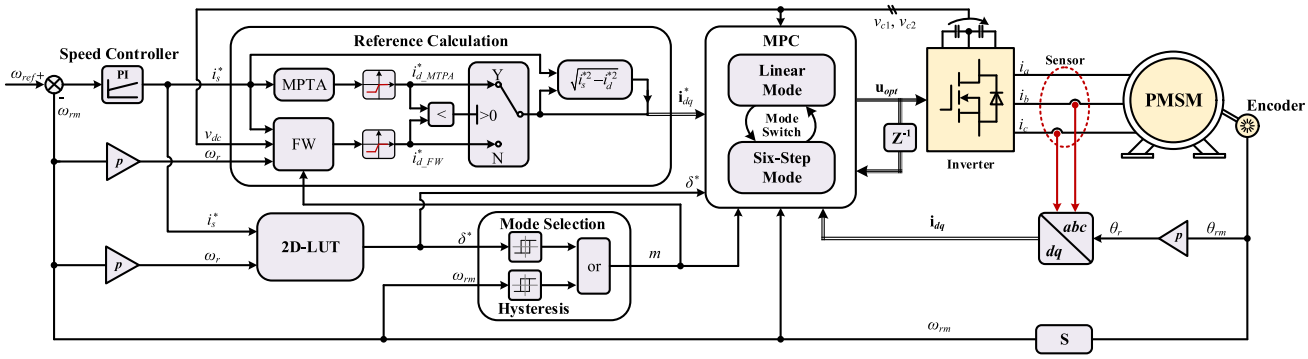

Fig. 8. Block diagram of the proposed MPC method illustrating reference calculation and mode selection.

hysteresis band is set for the speed ω_{rm} and the voltage angle δ^*. For example, if ω_{rm} is over ω_b and δ exceeds 90°, the operating mode will change from the linear MPC to the six-step MPC. When ω_{rm} is lower than $\omega_b - \varepsilon_\omega$ or δ^* is below $90° - \varepsilon_\delta$, the mode will change from the six-step MPC back to the linear MPC. Here, ε_ω and ε_δ are the hysteresis band values set for the rotor speed and the reference voltage angle, respectively. In this article, ε_ω is set to 10 rad/s, and ε_δ is set to 5°, which have been determined by simulations and experimentally to give sufficiently good results.

As shown in Fig. 8, the current reference calculation consists of a maximum torque per ampere (MTPA) block and a flux-weakening (FW) block. The linear control mode, as introduced in Section II-B, is used to operate under the rated motor speed, where the MTPA calculates the reference current [35].

The FW control is used to calculate the reference current to extend the operation of PMSM above the rated speed. Due to the absence of the modulation stage, there is no reference voltage that may be fed back to form the closed-loop FW control. In [24], the voltage magnitude is reconstructed from the current information and motor parameters. However, under the six-step operation, the six-order harmonics will be injected into the feedback and could lead to instability of the reference current. Alternatively, a feedforward method [36] is adopted in this article. According to this method, the current references are expressed by

$$i^*_{d\_\mathrm{FW}} = \frac{\psi_f L_d - \sqrt{(\psi_f L_d)^2 + (L_q^2 - L_d^2)\left[\psi_f^2 + L_q^2 i_s^{*2} - \left(\frac{v_{\max}}{\omega_r}\right)^2\right]}}{L_q^2 - L_d^2} \tag{35}$$

$$i^*_q = \sqrt{(i^*_s)^2 - (i^*_{d\_\mathrm{FW}})^2} \tag{36}$$

where $i^*_{d\_\mathrm{FW}}$ denotes the reference FW current of the d-axis; $v_{\max}$ represents the maximum available voltage, which depends on the operation mode of MPC (i.e., linear or six steps). Therefore, the value of $v_{\max}$ can be given as

$$v_{\max} = \begin{cases} \frac{1}{\sqrt{3}} v_{\mathrm{dc}}, & \text{if } m = 0 (\text{linear mode}) \\ \frac{2}{\pi} v_{\mathrm{dc}}, & \text{if } m = 1 (\text{six-step mode}). \end{cases} \tag{37}$$

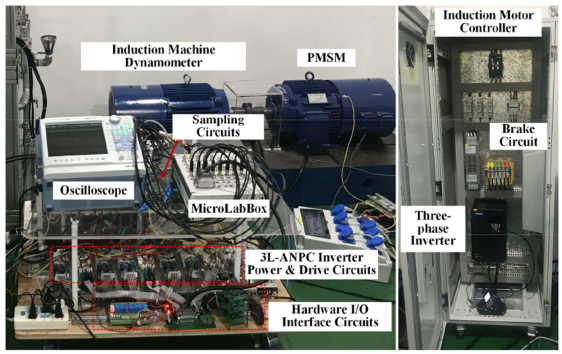

Fig. 9. Experimental setup used for implementation of the proposed method.

VI. Experimental Demonstrations

Extensive experimental studies have been conducted to evaluate the performance of the proposed method. Fig. 9 shows the hardware setup for the experiments, wherein an 11-kW interior PMSM is driven by a three-level active neutral point clamped inverter [16], [26] and an induction motor fed by a commercial variable frequency drive for applying the load torque. The dSPACE MircroLabBox serves as the controller for the PMSM. The parameters of the control system are summarized in the Appendix.

A. Steady-State Performance

This part evaluates the current-tracking performance with the proposed MPC method in a steady-state scenario of the six-step operation. To this end, the PMSM is controlled to operate at 800 r/min with a 10 N·m mechanical load. The measured results are presented in Figs. 10 and 11. Here, the comparisons are made among the conventional MPC (also for the linear mode), the proposed MPC with the forward Euler method, and the proposed MPC with the trapezoidal method.

First, for the conventional MPC in Figs. 10(a) and 11(a), the reference current is provided with a higher $v_{\max}$ ($2/\pi * v_{\mathrm{dc}}$) corresponding to the six-step mode. Although the phase current and phase voltage have reached a quasi-six-step operation, the q-axis current-tracking ability has been significantly reduced.

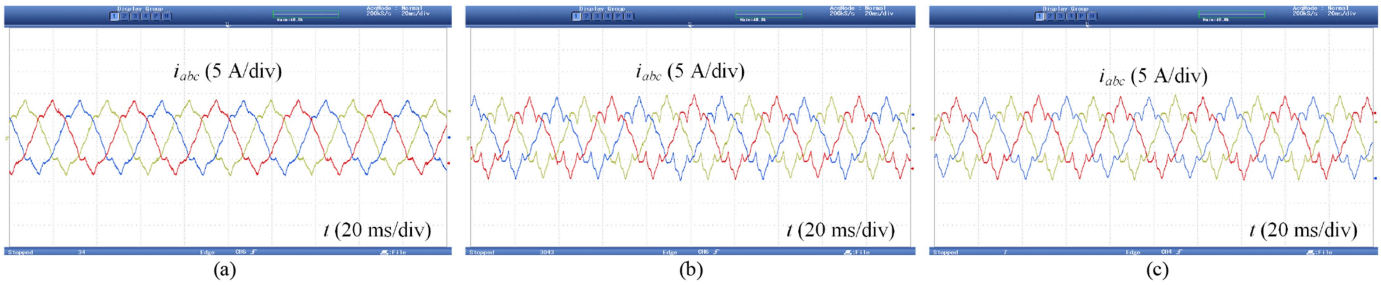

Fig. 10. Measured steady-state phase currents in overmodulation tests. (a) Conventional MPC. (b) Proposed MPC with forward Euler method. (c) Proposed MPC with trapezoidal method.

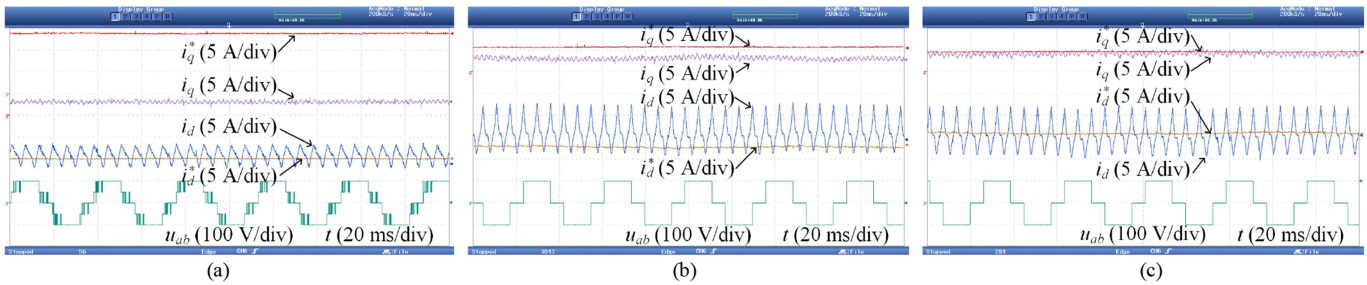

Fig. 11. Measured steady-state phase currents in dq coordinates and line-to-line voltages in overmodulation tests. (a) Conventional MPC. (b) Proposed MPC with forward Euler method. (c) Proposed MPC with trapezoidal method. The current tracking is achieved in (c), but not in (a) and (b).

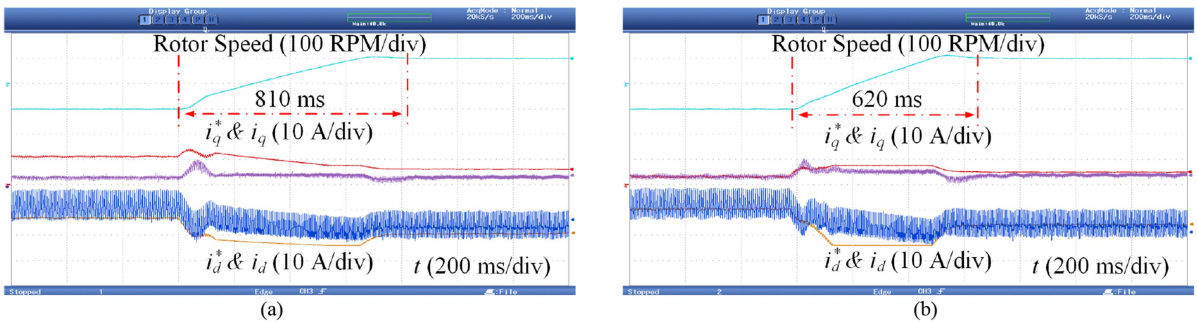

Fig. 12. Dynamic test results with reference rotor speed increased from 700 to 900 r/min. (a) Proposed MPC with the forward Euler method. (b) Proposed MPC with the trapezoidal method.

Furthermore, from the wave of line-to-line voltage, we can see that there are excessive switch transitions around the edge of voltage-level changes, which hinders the maximum dc-link voltage utilization of the conventional MPC. These results demonstrate that the overmodulation capability of the conventional MPC is limited.

As can be seen in Figs. 10(b) and (c) and 11(b) and (c), the performance of the proposed MPC is validated in terms of phase current and line voltage. These results demonstrate that the proposed MPC method has good overmodulation capability and extends the six-step operation. From the comparison between the two discretization methods, it is seen that the trapezoidal method in Figs. 10(c) and 11(c) demonstrates more accurate reference current tracking than the performance of the forward Euler method in Figs. 10(b) and 11(b). The current i_q in Fig. 11(b) is slightly lower than its reference, which is consistent with the analysis, as presented in Section V-A.

B. Dynamic Performance

In this study, the dynamic performance with respect to the speed and load change scenarios of the proposed method is evaluated, and comparisons are made between the forward Euler method and the trapezoidal method. The results are presented in Fig. 12, wherein the speed reference steps from 700 to 900 r/min. The coefficient ε for the voltage vector clamping is set to $\pi/18$ in this case; thus, the maximum advance angle of the voltage is 10°. Due to the higher current-tracking accuracy, the trapezoidal

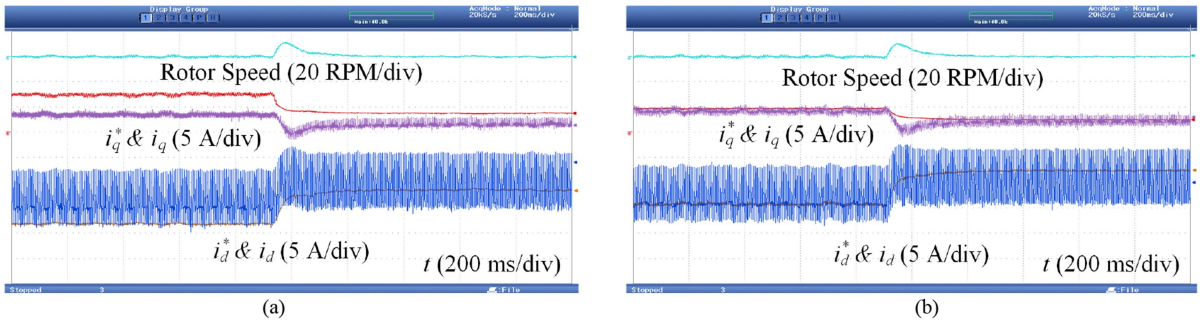

Fig. 13. Dynamic tests result with load torque steps from 10 to 2 N·m. (a) Proposed MPC with the forward Euler method. (b) Proposed MPC with the trapezoidal method.

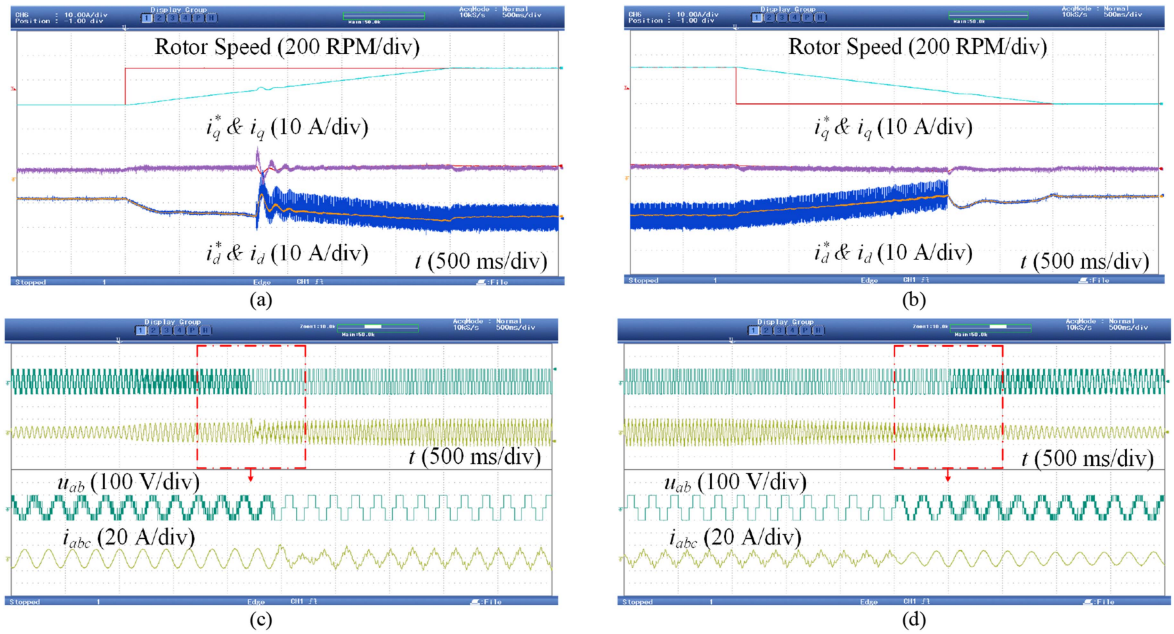

Fig. 14. Dynamic tests result of mode switch scenarios corresponding to rotor speed ramping up from 600 to 900 r/min, and then ramping down from 900 to 600 r/min using the proposed MPC with a trapezoidal method. (a) and (b) Performance of rotor speed and dq-axis currents. (c) and (d) Performance of line-to-line voltage and phase current.

method achieves faster current responses, significantly reducing the speed step time.

Fig. 13 presents the transient performance resulting from the load torque changes from 10 to 2 N·m. The nearly identical responses can be seen from the figure for the proposed MPC with two different discretization methods. Nevertheless, the forward Euler method shows larger current-tracking errors than the error with the trapezoidal method in the whole time range.

To validate the mode switch performance, the PMSM works from the linear speed region to the flux-weakening region, which is presented in Fig. 14. The conventional linear MPC and the proposed MPC with the trapezoidal method are adopted in this scenario. The reference speed is set to change from 600 to 900 r/min and then set back to 600 r/min, while the rotor speed slew rate is limited to ± 100 r/min in this case. It is seen that the dq-axis current can accurately and rapidly track the reference in the entire speed range. No significant speed and current overshoots are seen during the control-mode switching.

C. Computational Cost

The execution time for different control algorithms has been measured in real time on the considered microprocessor and is illustrated in Fig. 15. The number of prediction steps z for the six-step mode is set as 10 in the tests. Although the alternative voltage vectors with the six-step control mode are reduced from 27 to 2, Fig. 15 shows that the multistep prediction consumes a lot of computational resources. It can be seen that the microprocessor execution time for the MPC with linear mode is around 26 μs. The execution time for the MPC operating in the six-step mode depends on the voltage clamping. When the optimization process with MPC is activated to decide the optimal commutation instant, the microprocessor execution time

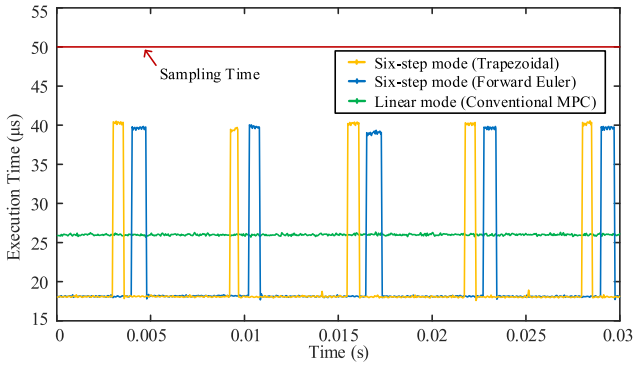

Fig. 15. Microprocessor execution time of different methods in the experimental implementation.

becomes high, reaching up to 40 μs. During other times, when no current predictions are made, the execution time drops down to 18 μs. In addition, from the comparison in Fig. 15, we can see that using the trapezoidal method only slightly increases the computing cost compared with the forward Euler method. This demonstrates the advantages of using the trapezoidal method.

VII. Conclusion

This article presents an improved MPC method that has been extended for the six-step operation of traction PMSM drives. The proposed method derives a new objective function using the average value of phase current and combines trapezoidal method-based multistep prediction to enhance the current-tracking accuracy and overall control performance. The experimental results demonstrate the effectiveness of the proposed method and the ability to transition smoothly between the linear and the six-step modes, which may not be possible with the conventional MPC methods. The multistep long-term prediction combined with the trapezoidal discretization appears to achieve good current-tracking results for the six-step operation while only slightly increasing the computational cost compared with the forward Euler method. The proposed control method overall may be very useful for traction drives, enabling increased dc-link voltage utilization in the high-speed region.

Appendix

A. Parameters of PMSM

$P = 11$ kW, $U = 380$ V, $N_r = 1500$ r/min, $p = 2$, $R_s = 0.383\,\Omega$, $L_d = 11.2$ mH, $L_q = 27.5$ mH, and $\psi_f = 0.77$ Wb.

B. Parameters of the Inverter

$C_{\mathrm{dc}} = 6$ mF and $v_{\mathrm{dc}} = 200$ V.

C. Parameters of the Controller

$T_s = 50\ \mu$s, $k_p = 0.3$, $k_i = 6$, $z = 10$, $\varepsilon = \pi/18$, $\varepsilon_\omega = 10$ rad/s, and $\varepsilon_\delta = 5°$.

D. Setup Details

Controller: dSpace MicroLabBox. Semiconductor modules of the ANPC inverter: Infeneon FF200R12KE3, CREE CAS120M12BM2. Commercial inverter for load: Inovance MD520.

References

[1] G. Pellegrino, A. Vagati, P. Guglielmi, and B. Boazzo, "Performance comparison between surface-mounted and interior PM motor drives for electric vehicle application," *IEEE Trans. Ind. Electron.*, vol. 59, no. 2, pp. 803–811, Feb. 2012.

[2] V. T. Buyukdegirmenci, A. M. Bazzi, and P. T. Krein, "Evaluation of induction and permanent-magnet synchronous machines using drive-cycle energy and loss minimization in traction applications," *IEEE Trans. Ind. Appl.*, vol. 50, no. 1, pp. 395–403, Jan./Feb. 2014.

[3] Y. Yang et al., "Design and comparison of interior permanent magnet motor topologies for traction applications," *IEEE Trans. Transp. Electrific.*, vol. 3, no. 1, pp. 86–97, Mar. 2017.

[4] J. Holtz, W. Lotzkat, and A. M. Khambadkone, "On continuous control of PWM inverters in the overmodulation range including the six-step mode," *IEEE Trans. Power Electron.*, vol. 8, no. 4, pp. 546–553, Oct. 1993.

[5] Y.-C. Kwon, S. Kim, and S.-K. Sul, "Six-step operation of PMSM with instantaneous current control," *IEEE Trans. Ind. Appl.*, vol. 50, no. 4, pp. 2614–2625, Jul./Aug. 2014.

[6] J. Zhou, S. Ebrahimi, and J. Jatskevich, "Extended operation of brushless DC motors beyond 120° under maximum torque per ampere control," *IEEE Trans. Energy Convers.*, vol. 38, no. 2, pp. 1280–1291, Jun. 2023.

[7] Y. Zhang, M. K. Güven, S. Chi, and M. Illindala, "Experimental verification of deep field weakening operation of a 50-kW IPM machine by using single current regulator," *IEEE Trans. Ind. Appl.*, vol. 47, no. 1, pp. 128–133, Jan./Feb. 2011.

[8] D. Zhang, M. Zhou, C. Wang, and X. You, "A single-current-regulator flux-weakening control for PMSM under square-wave mode with wider operation range," *IEEE Trans. Transp. Electrific.*, vol. 8, no. 1, pp. 1063–1071, Mar. 2022.

[9] Z. Zhang, C. Wang, M. Zhou, and X. You, "Flux-weakening in PMSM drives: Analysis of voltage angle control and the single current controller design," *IEEE J. Emerg. Sel. Topics Power Electron.*, vol. 7, no. 1, pp. 437–445, Mar. 2019.

[10] T. Miyajima, H. Fujimoto, and M. Fujitsuna, "A precise model-based design of voltage phase controller for IPMSM," *IEEE Trans. Power Electron.*, vol. 28, no. 12, pp. 5655–5664, Dec. 2013.

[11] S. Kim and J.-K. Seok, "Maximum voltage utilization of IPMSMs using modulating voltage scalability for automotive applications," *IEEE Trans. Power Electron.*, vol. 28, no. 12, pp. 5639–5646, Dec. 2013.

[12] J. Liu, W. Zhang, F. Xiao, C. Lian, and S. Gao, "Six-step mode control of IPMSM for railway vehicle traction eliminating the DC offset in input current," *IEEE Trans. Power Electron.*, vol. 34, no. 9, pp. 8981–8993, Sep. 2019.

[13] H.-J. Cho, Y.-C. Kwon, and S.-K. Sul, "Time-optimal voltage vector transition scheme for six-step operation of PMSM," *IEEE Trans. Power Electron.*, vol. 36, no. 5, pp. 5724–5735, May 2021.

[14] S. Vazquez, J. Rodriguez, M. Rivera, L. G. Franquelo, and M. Norambuena, "Model predictive control for power converters and drives: Advances and trends," *IEEE Trans. Ind. Electron.*, vol. 64, no. 2, pp. 935–947, Feb. 2017.

[15] J. Rodriguez et al., "Latest advances of model predictive control in electrical drives—Part I: Basic concepts and advanced strategies," *IEEE Trans. Power Electron.*, vol. 37, no. 4, pp. 3927–3942, Apr. 2022.

[16] Z. Sun, S. Xu, G. Ren, C. Yao, G. Ma, and J. Jatskevich, "Weighting-factor-less model predictive control with multiobjectives for three-level hybrid ANPC inverter drives," *IEEE J. Emerg. Sel. Topics Power Electron.*, vol. 11, no. 5, pp. 4726–4738, Oct. 2023.

[17] F. Wang, Y. Wei, H. Young, D. Ke, H. Xie, and J. Rodriguez, "Continuous-control-set model-free predictive fundamental current control for PMSM system," *IEEE Trans. Power Electron.*, vol. 38, no. 5, pp. 5928–5938, May 2023.

[18] A. Sarajian et al., "Overmodulation methods for modulated model predictive control and space vector modulation," *IEEE Trans. Power Electron.*, vol. 36, no. 4, pp. 4549–4559, Apr. 2021.

[19] J. Yun, J. Yoo, S. Cui, and S.-K. Sul, "Model predictive control for six-step operation of PMSM based on adapted fast gradient method," *IEEE Trans. Power Electron.*, vol. 38, no. 5, pp. 5952–5962, May 2023.

[20] P. Karamanakos and T. Geyer, "Guidelines for the design of finite control set model predictive controllers," *IEEE Trans. Power Electron.*, vol. 35, no. 7, pp. 7434–7450, Jul. 2020.
[21] Z. Mynar, L. Vesely, and P. Vaclavek, "PMSM model predictive control with field-weakening implementation," *IEEE Trans. Ind. Electron.*, vol. 63, no. 8, pp. 5156–5166, Aug. 2016.
[22] Y. Zhang, B. Zhang, H. Yang, M. Norambuena, and J. Rodriguez, "Generalized sequential model predictive control of IM drives with field-weakening ability," *IEEE Trans. Power Electron.*, vol. 34, no. 9, pp. 8944–8955, Sep. 2019.
[23] H. Yang, Y. Zhang, and W. Shen, "Predictive current control and field-weakening operation of SPMSM drives without motor parameters and DC voltage," *IEEE J. Emerg. Sel. Topics Power Electron.*, vol. 10, no. 5, pp. 5635–5646, Oct. 2022.
[24] Q. Dong, B. Wang, L. Xia, Y. Yu, M. Tian, and D. Xu, "A virtual voltage field-weakening scheme of trajectory correction for PMSM model predictive control," *IEEE Trans. Power Electron.*, vol. 38, no. 3, pp. 3044–3056, Mar. 2023.
[25] T. Geyer, "Computationally efficient model predictive direct torque control," *IEEE Trans. Power Electron.*, vol. 26, no. 10, pp. 2804–2816, Oct. 2011.
[26] Z. Sun, G. Ma, S. Xu, H. Zhang, and G. Ren, "Reduced vector model predictive control of ANPC inverter for PMSM drives with optimized commutation," *IEEE Trans. Transp. Electrific.*, vol. 8, no. 3, pp. 3177–3191, Sep. 2022.
[27] X. Fang, S. Lin, X. Wang, Z. Yang, F. Lin, and Z. Tian, "Model predictive current control of traction permanent magnet synchronous motors in six-step operation for railway application," *IEEE Trans. Ind. Electron.*, vol. 69, no. 9, pp. 8751–8759, Sep. 2022.
[28] J. Holtz, "Advanced PWM and predictive control—An overview," *IEEE Trans. Ind. Electron.*, vol. 63, no. 6, pp. 3837–3844, Jun. 2016.
[29] J. Holtz, "Predictive finite-state control—When to use and when not," *IEEE Trans. Power Electron.*, vol. 37, no. 4, pp. 4225–4232, Apr. 2022.
[30] S. Zhao, X. Huang, Y. Fang, and H. Zhang, "DC-link-fluctuation-resistant predictive torque control for railway traction permanent magnet synchronous motor in the six-step operation," *IEEE Trans. Power Electron.*, vol. 35, no. 10, pp. 10982–10993, Oct. 2020.
[31] T. Geyer and D. E. Quevedo, "Performance of multistep finite control set model predictive control for power electronics," *IEEE Trans. Power Electron.*, vol. 30, no. 3, pp. 1633–1644, Mar. 2015.
[32] P. Acuna, C. A. Rojas, R. Baidya, R. P. Aguilera, and J. E. Fletcher, "On the impact of transients on multistep model predictive control for medium-voltage drives," *IEEE Trans. Power Electron.*, vol. 34, no. 9, pp. 8342–8355, Sep. 2019.
[33] Z. Sun, S. Xu, G. Ma, and J. Jatskevich, "Improved multistep model predictive control for six-step operation of traction PMSM drives," in *Proc. IEEE Int. Conf. Predictive Control Elect. Drives Power Electron.*, 2023, pp. 1–6, doi: 10.1109/PRECEDE57319.2023.10174516.
[34] W. Xie, X. Wang, F. Wang, W. Xu, R. Kennel, and D. Gerling, "Dynamic loss minimization of finite control set-model predictive torque control for electric drive system," *IEEE Trans. Power Electron.*, vol. 31, no. 1, pp. 849–860, Jan. 2016.
[35] A. Dianov, F. Tinazzi, S. Calligaro, and S. Bolognani, "Review and classification of MTPA control algorithms for synchronous motors," *IEEE Trans. Power Electron.*, vol. 37, no. 4, pp. 3990–4007, Apr. 2022.
[36] J. Wang, J. Wu, C. Gan, and Q. Sun, "Comparative study of flux-weakening control methods for PMSM drive over wide speed range," in *Proc. 19th Int. Conf. Elect. Mach. Syst.*, 2016, pp. 1–6.

Zhenyao Sun (Student Member, IEEE) received the B.Sc. and M.Sc. degrees in vehicle engineering from Beijing Forestry University, Beijing, China, and Xihua University, Chengdu, China, in 2015 and 2019, respectively. He is currently working toward the Ph.D. degree with the State Key Laboratory of Rail Transit Vehicle System, Southwest Jiaotong University, Chengdu, China.

From 2022 to 2023, he was a joint Ph.D. student with The University of British Columbia, Vancouver, BC, Canada. His research interests include advanced control for multilevel power converters and electric motor drives.

Guanzhou Ren received the B.Sc. degree in traffic equipment and control engineering in 2020 from Southwest Jiaotong University, Chengdu, China, where he is currently working toward the Ph.D. degree in vehicle application engineering with the State Key Laboratory of Rail Transit Vehicle System.

His research interests include the traction motor control algorithm and PMSM modulation algorithm.

Shuai Xu (Member, IEEE) received the B.Sc. and M.Sc. degrees from Henan Polytechnic University, Jiaozuo, China, in 2011 and 2013, respectively, and the Ph.D. degree from Southeast University, Nanjing, China, in 2018, all in electrical engineering.

From 2016 to 2017, he was a joint Ph.D. student with The University of British Columbia, Vancouver, BC, Canada. Since 2019, he has been with the State Key Laboratory of Rail Transit Vehicle System, Southwest Jiaotong University, Chengdu, China, where he is currently an Associate Professor. His research interests include multilevel converters, motor drives, fault diagnosis, and fault-tolerant control.

Guangtong Ma (Member, IEEE) received the B.E. and Ph.D. degrees in electrical engineering from Southwest Jiaotong University (SWJTU), Chengdu, China, in 2005 and 2009, respectively.

From 2011 to 2013, he was an Alexander von Humboldt Research Fellow with Technische Universität Darmstadt, Darmstadt, Germany. Since 2010, he has been with the State Key Laboratory of Rail Transit Vehicle System, SWJTU, where he is currently a Full Professor and the Deputy Director. His research interests include superconducting levitation, linear motor, and traction motor.

Juri Jatskevich (Fellow, IEEE) received the M.S.E.E. and Ph.D. degrees in electrical engineering from Purdue University, West Lafayette, IN, USA, in 1997 and 1999, respectively.

Since 2002, he has been with The University of British Columbia, Vancouver, BC, Canada, where he is currently a Professor with the Department of Electrical and Computer Engineering. His research interests include power electronic systems, electrical machines and drives, and modeling and simulation of electromagnetic transients.

Dr. Jatskevich served as an Associate Editor for IEEE TRANSACTIONS ON POWER ELECTRONICS from 2008 to 2013, the Editor-in-Chief for IEEE TRANSACTIONS ON ENERGY CONVERSION from 2013 to 2019, and the Editor-in-Chief At-Large for *IEEE PES Journals* in 2019 and 2020. He is also chairing IEEE Task Force on Dynamic Average Modeling, under the Working Group on Modeling and Analysis of System Transients Using Digital Programs. He was the recipient of the 2022 IEEE PES Cyril Veinott Electromechanical Energy Conversion Award.